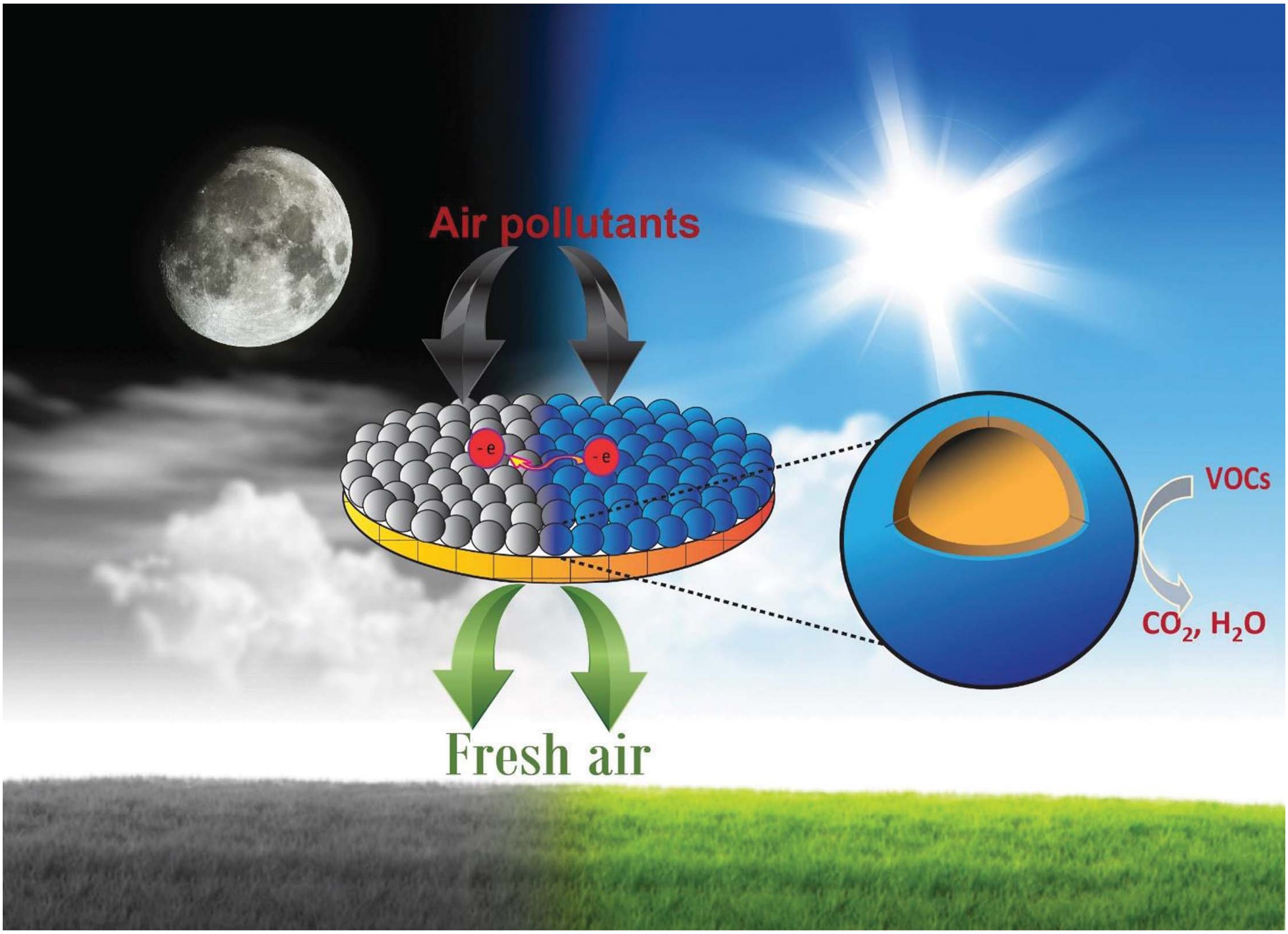

Showcasing research from the Nanomaterials & Photocatalysis Lab of the Department of Chemical Engineering, Laval University, Quebec, Canada.

Title: Efficient hollow double-shell photocatalysts for the degradation of organic pollutants under visible light and in darkness

The development of photocatalysts that can work both under visible light and in darkness remains an important research target for environmental applications. This report presents the first synthesis of hollow double-shell H:Pt–WO_3/TiO_2–Au nanospheres that exhibit efficient degradation of organic pollutants both under visible light and in darkness. This work opens a new approach to develop efficient 24 hour-working photocatalysts for air purification and waste water treatment.

As featured in:

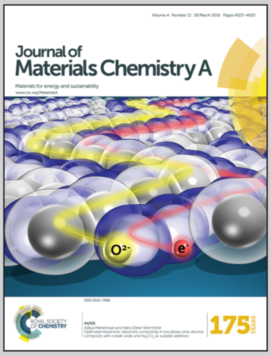

See Trong-On Do *et al.*,
J. Mater. Chem. A, 2016, **4**, 4413.

www.rsc.org/MaterialsA

Registered charity number: 207890

Journal of
Materials Chemistry A

PAPER

Cite this: *J. Mater. Chem. A*, 2016, **4**, 4413

Efficient hollow double-shell photocatalysts for the degradation of organic pollutants under visible light and in darkness†

Chinh-Chien Nguyen, Nhu-Nang Vu and Trong-On Do*

Received 7th November 2015
Accepted 21st December 2015

DOI: 10.1039/c5ta09016d

www.rsc.org/MaterialsA

The development of efficient photocatalysts that can work both under visible light and in darkness remains an important research target for environmental applications. A large number of photocatalysts have been reported, but they still suffer from low activity that originates from fundamental efficiency bottlenecks: *i.e.*, weak photon absorption and poor electron–hole pair separation when operating under irradiation, and poor electron storage capacity when operating in darkness. Herein, we report the first synthesis of hollow double-shell H:Pt–WO_3/TiO_2–Au nanospheres with high specific surface area, large TiO_2/WO_3 interfacial contact and strong visible light absorption. Because of these features, this type of nanocomposite shows high charge separation and electron storage capacity, and exhibits efficient degradation of organic pollutants both under visible light ($\lambda \geq 420$ nm) and in darkness. In addition, CO_2 generation from formaldehyde gave a high quantum efficiency of 77.6%.

Introduction

Semiconductor-based photocatalysts are attractive candidates for clean energy production and for environmental applications, such as air purification and wastewater treatment. TiO_2, one of the most widely used semiconducting metal oxides, has received enormous research interest in the past few decades, due to its exceptional ability to decompose organic pollutants, as well as its corrosion resistance, durability, nontoxicity, and low cost.[1,2] Unfortunately, the application of TiO_2 is limited to UV light, which makes up only ~4% of the energy of the incident solar spectrum.[3,4] To overcome this limitation, research efforts have been focused on the development of photocatalysts with strong visible-light absorption, which accounts for 43% of the energy of the solar spectrum. However, the developed materials still suffer from two fundamental drawbacks: weak photon absorption and poor electron–hole pair separation.[5]

To overcome the drawbacks of photocatalysts that only function under light illumination, the development of a photocatalytic system that can work both under light irradiation and in darkness is urgently required. The underlying concept is the coupling of a semiconductor (as an electron generator) with another substance (as an electron acceptor), wherein the semiconductor provides photo-excited electrons under light irradiation and the coupled substance receives and stores the electrons; the stored electrons are subsequently released in darkness for organic pollutant decomposition.[6] Despite several reports by Fujishima *et al.* relating to a photocatalyst based on the WO_3/TiO_2 heterostructure, few systems exhibiting the desired functionality have been reported.[7–10] As seen in Scheme SI-1,† due to the matching band energy levels, excited electrons from the conduction band of TiO_2 can be transferred to that of WO_3, wherein the electrons could be stored for reaction in darkness.[6,8–10] It should be noted that the minimal WO_3/TiO_2 heterostructure interface prepared by conventional methods restricts both charge separation and electron storage capacity. Also, this system absorbs only UV light, meaning its photocatalytic activity under visible light and electron charge–discharge behaviour were both poor. Therefore, to use solar energy more efficiently, photocatalysts that absorb the entire solar spectrum and possess high electron storage ability must be developed.

The use of plasmonic nanoparticles (NPs) and surface modification are the main methods that have been proposed to achieve this enhancement.[11,12] Au, Ag, and Cu NPs can harvest visible light through surface plasmon resonance (SPR) to produce "hot" electrons on their surfaces.[13] These "hot" electrons can transfer to the neighbouring semiconductor for participation in chemical reactions *via* an interface, thereby enhancing catalyst efficiency.[14,15] Of these metal NPs, Au NPs most strongly absorb visible light and efficiently catalyse the decomposition of organic pollutants.[16] In addition, surface modification through hydrogen treatment to introduce oxygen vacancies can create impurity states in forbidden areas of the band structure, leading to improved photoabsorption and electron storage. Hence, this strategy provides an efficient route to the development of functional materials.[17]

Department of Chemical Engineering, Laval University, Quebec, G1V 0A8, Canada. E-mail: trong-on.do@gch.ulaval.ca; Fax: +1-418-656-5993; Tel: +1-418-656-3774

† Electronic supplementary information (ESI) available. See DOI: 10.1039/c5ta09016d

Nanocomposite-based hollow structure photocatalysts have recently attracted much research attention because of their unique properties, *viz.* their nanoscale wall thickness, large interface between components, which play a critical role in photogenerated charge transfer, and high porosity within the walls, which reduces the diffusion length and improves the accessibility of active sites for the reactants.[18,19] Additionally, multiple reflections within the hollow cavity enhance the efficient use of the light source, leading to the production of more photogenerated charge carriers.[20]

In this study, we developed a new type of hollow double-shell photocatalyst based on our recently developed approach.[21,22] This new type of hollow photocatalyst consists of two components: (i) an electron storage material (Pt–WO_3) and (ii) an electron generator (TiO_2–Au); herein, hollow double-shells are formed and two metal NPs (Pt as a co-catalyst and Au as a strong visible-light SPR absorber) are selectively loaded onto WO_3 and TiO_2, respectively. This material is then treated with hydrogen to enlarge its light absorption spectrum and to create trapping sites that allow electron storage. This type of hollow double-shell nanocomposite has unique properties, such as high specific surface area, large TiO_2/WO_3 interfacial contact, strong sunlight absorption, high electron–hole separation, and large electron storage capacity. As a result, the prepared material showed excellent activity for the degradation of formaldehyde (HCHO), a major indoor air pollutant, under visible light and in darkness.

Results and discussion

The production of this photocatalyst begins with the one-pot synthesis of Pt–WO_3/carbon core–shell nanospheres, which are subsequently coated with titanate nanodisk (TND) titania precursors using a layer-by-layer technique employing poly(ethyleneimine) (PEI) as a polyelectrolyte.[18,23] Due to the negatively charged surface of carbonaceous nanospheres (carbon core), the positively charged PEI easily binds to the carbon core *via* electrostatic forces, and converts into a positively charged core surface.[19,24,25] Subsequently, negatively charged TNDs are adsorbed. The layer-by-layer technique combined with the uniform size of TNDs allows the tuning of shell thickness. The Au precursor ($AuCl_4^-$) is then loaded on carbon core@Pt–WO_3/TNDs to produce carbon core@Pt–WO_3/TNDs–$AuCl_4^-$ (see the Experimental Section in the ESI† for details). In the second step, the carbon cores and other organic compounds are removed from the obtained core–shell nanospheres by calcination in air to form hollow Pt–WO_3/TiO_2–Au nanospheres (namely Pt–WO_3/TiO_2–Au), which then undergo H_2 treatment to afford the H_2-treated hollow double-shell Pt–WO_3/TiO_2–Au nanospheres (denoted as H:Pt–WO_3/TiO_2–Au), as depicted in Fig. 1 and Scheme SI2.†

It is worth noting that the calcination step in the synthesis is significant, as it generates microporosity in the shells by removing the carbon core and PEI. This microporosity promotes hydrogen contact with the TiO_2 and WO_3 surfaces and thereby lowers the required H_2 treatment temperature. In this way, high specific surface area, large TiO_2/WO_3 interface, strong visible light absorption, effective charge separation, and high electron storage capacity can be achieved. To the best of our knowledge, this is the first synthesis of this type of hollow double-shell H_2-treated WO_3/TiO_2 nanocomposite based on carbon colloidal spheres combined with the layer-by-layer technique.

Fig. 2A and B show scanning electron microscopy (SEM) images of the Pt–WO_3/TiO_2–Au core–shell sample before (A) and after calcination and subsequent H_2 treatment (B). The nanospheres are quite uniform, with an average diameter of 1 μm. A slight change in morphology is observed before the carbon colloidal core is removed and after hydrogen treatment. As seen in Fig. 2B, some broken particles clearly indicate the presence of the hollow nanospheres. These might be formed during calcination for carbon core removal. The presence of these holes, in fact, should be beneficial for photocatalysis as they enhance the diffusion of reactants and light through the shell of the hollow spheres (*vide infra*).[26,27] The morphology of the hollow H:Pt–WO_3/TiO_2–Au sample was further characterized by transmission electron microscopy (TEM) (Fig. 2C and D). Hollow spheres of ~1 μm in average diameter were observed (Fig. 2C). Moreover, Au NPs with an average size of 22 nm are evenly distributed on the wall surface of the TiO_2 HNSs (Fig. 2D) while Pt NPs are not observed, probably due to the Pt particles being small and highly dispersed in the hollow nanocomposite. The

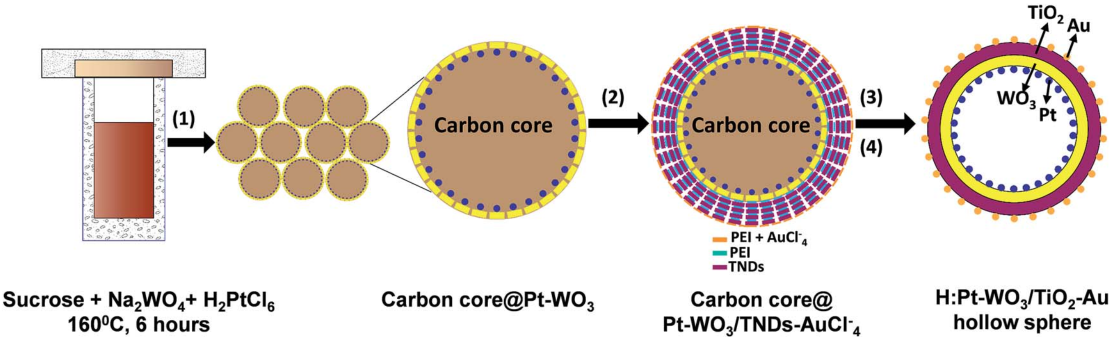

Fig. 1 Schematic illustration of the synthesis of hollow double-shell H:Pt–WO_3/TiO_2–Au nanospheres: (1) one-pot synthesis of Pt–WO_3@-carbon colloidal spheres, (2) coating with TNDs using a layer-by-layer strategy followed by Au precursor loading, (3) calcination at 550 °C for 3 h, and (4) hydrogen treatment at 350 °C for 1 h.

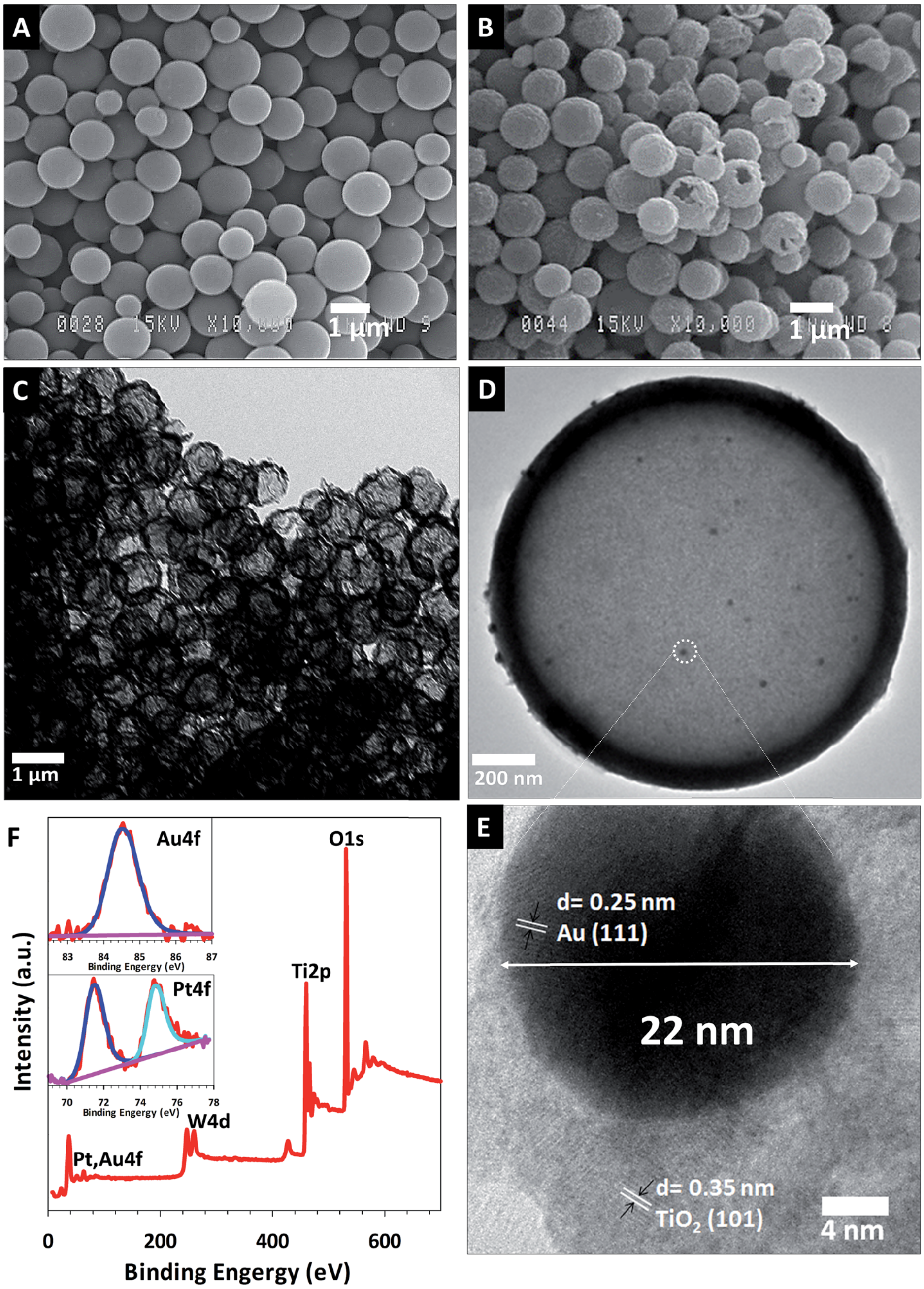

Fig. 2 (A and B) SEM images of Pt–WO_3/TiO_2–Au before and after calcination followed by hydrogen treatment; (C and D) TEM image of the hollow H:Pt–WO_3/TiO_2–Au; (E) high resolution TEM image of hollow H:Pt–WO_3/TiO_2–Au; (F) survey spectrum of hollow H:Pt–WO_3/TiO_2–Au, inset XPS of Au and Pt.

thickness of the HNS shell is estimated to be around 80 nm. The high-resolution TEM image (Fig. 2E) shows the lattice fringes of both TiO_2 and Au, thus indicating the highly crystalline nature of TiO_2 and the Au NPs. The lattice fringe with a *d*-spacing of 0.35 nm can be assigned to the (101) lattice plane of anatase TiO_2, and the fringe with a *d*-spacing of 0.25 nm belongs to the (111) lattice plane of Au with a face-centred cubic phase.[28] Fig. 2E also shows intimate contact between Au and TiO_2. This close contact between the metal and the semiconductor may enhance charge transfer between them, and consequently the photocatalytic efficiency.[29,30] As seen in Fig. SI-1,† significant shrinking of the hollow area of H:Pt–WO_3 (~500 nm in size) without coated TNDs was observed. Therefore, it should be noted that the coated TNDs play the critical role of maintaining the spherical shape after calcination and hydrogen treatment. Fig. 2F shows the X-ray photoelectron spectroscopy (XPS) spectrum of the hollow H:Pt–WO_3/TiO_2–Au spheres. The photoelectron peaks for Ti 2p and W 4d appear clearly at binding energies of 460 and 248 eV, respectively. As seen in the inset of Fig. 2F, the Pt XPS spectra show two peaks at 71.41 and

74.76 eV attributed to metallic Pt, confirming the presence of Pt in the sample, while the Au 4f XPS spectra exhibit a peak at 84.4 eV characteristic of Au^0 on TiO_2.[31] Elemental analysis by inductively coupled plasma mass spectrometry (ICP-MS) reveals that the Au and Pt loadings are 3.0 and 2.5 wt%, respectively. The H:Pt–WO_3/TiO_2–Au sample was also analysed by energy-dispersive spectroscopy (EDS), as shown in Fig. SI2.† The EDS spectra clearly show that W and Ti are the main constituent elements and that the atomic W : Ti ratio is around 1 : 1 in the nanocomposite.

The X-ray diffraction pattern of the hollow double-shell H:Pt–WO_3/TiO_2–Au sample is shown in Fig. 3A, indicating the presence of WO_3, TiO_2, and Au in the material; no XRD peak characteristic of Pt was detected. As mentioned above, this could be due to the small size of the Pt NPs (<5 nm). The WO_3 phase is confirmed by the peak at $2\theta = 23°$. The peak at $2\theta = 25.2°$ matches well with the anatase phase of TiO_2,[32] while the peak at 38.5° corresponds to the (111) plane of Au.[33] Meanwhile, the intensities of the WO_3 and TiO_2 phases in the XRD patterns are relatively weak because of the NP size and the increase in the WO_3/TiO_2 interface in the nanocomposite.[34–36] Fig. 3B shows the UV-vis absorption spectra of different calcined hollow samples before and after H_2 treatment: hollow Pt–WO_3/TiO_2 in the absence of Au, Pt–WO_3/TiO_2–Au (both before H_2 treatment), hollow H:Pt–WO_3, hollow H:Pt–WO_3/TiO_2, and hollow H:Pt–WO_3/TiO_2–Au (after H_2 treatment). For the samples untreated with H_2 (Fig. 3B(a and b)), the UV-vis spectra are mostly identical, except for a peak centred at 550 nm that is attributed to the SPR of Au NPs in the Pt–WO_3/TiO_2–Au sample.[14] Interestingly, after H_2 treatment, all the samples show strong and broad light absorption, extending to even the NIR region (Fig. 3B(c–e)). These indicate the full sunlight absorption of these samples after H_2 treatment, which is in agreement with the colour change from pink to dark green (Pt–WO_3/TiO_2 and Pt–WO_3/TiO_2–Au), and from yellow to black (hollow H:Pt–WO_3) after hydrogen treatment. It should be noted that the presence of Pt NPs on WO_3 has a significant impact on reduction by hydrogen. Facile reduction and change in colour of WO_3 during H_2 treatment could be a result of the chemisorption and subsequent dissociation of H_2 molecules on the Pt NP surface to very active hydrogen atoms (*i.e.*, hydrogen spillover). These hydrogen atoms then migrate to the WO_3 particles, reducing them to black WO_{3-x} particles.[37] In contrast, no significant change in colour or in the UV-vis spectra was observed for the samples without Pt, neither before nor after H_2 treatment (see Fig. SI-3† for details).

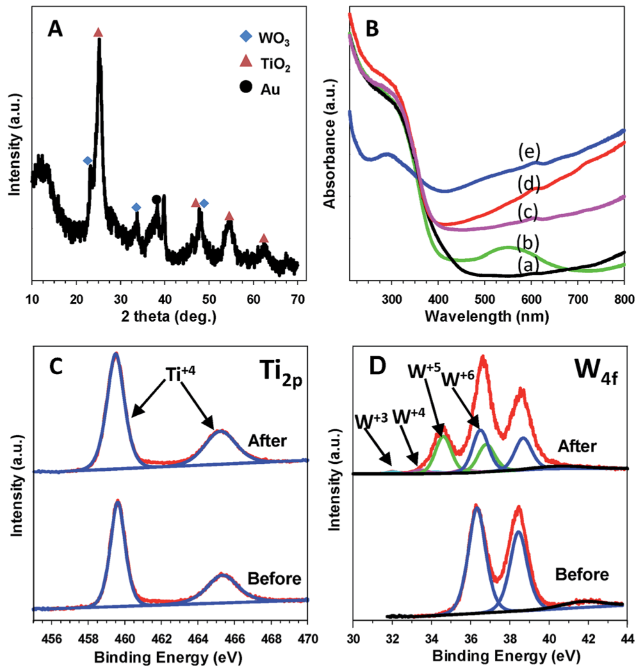

Fig. 3 (A) Powder XRD spectrum of hollow H:Pt–WO_3/TiO_2–Au; (B) UV-vis spectra of different samples: (a) hollow Pt–WO_3/TiO_2, (b) hollow Pt–WO_3/TiO_2–Au before H_2 treatment; (c) hollow H:Pt–WO_3/TiO_2, (d) hollow H:Pt–WO_3/TiO_2–Au, and (e) hollow H:Pt–WO_3 after hydrogen treatment; (C and D) XPS Ti 2p and W 4f spectra of Pt–WO_3/TiO_2–Au before and after H_2 treatment.

The surface chemical states of Ti and W before and after hydrogen annealing were characterized by X-ray photoelectron spectroscopy (XPS). Fig. 3C shows the Ti $2p_{3/2}$ XPS spectra of these samples. The Ti $2p_{3/2}$ XPS spectrum of the sample before H_2 treatment shows two peaks at the binding energies of 458.4 eV and 464.1 eV, which are characteristic of Ti^{4+} in anatase TiO_2. The similarities between the obtained Ti $2p_{3/2}$ spectra indicate a similar bonding environment after hydrogen treatment.[38,39] The W 4f XPS spectra of these samples are shown in Fig. 3D. For the sample before H_2 treatment, only two XPS peaks at 38.4 and 36.3 eV were found, which are characteristic of W^{6+}. However, after H_2 treatment, the sample exhibits different oxidation states for W. Apart from the two main XPS peaks for W^{6+} at 38.4 and 36.3 eV, the appearance of W^{5+} and W^{4+} is unambiguously observed in the H_2-treated sample. As seen in Fig. 3D, the two peaks located at 34.5 and 36.4 eV are assigned to W^{5+}, and the two peaks centred at 32.1 and 33.5 eV are attributed to W^{4+} species; small peaks at 32.0 and 34.2 eV characteristic of W^{3+} were also found. It should be noted that the WO_3 chemical states could be observed in the as-prepared sample due to the presence of Pt NPs on the WO_3. The dissociation of H_2 molecules on Pt NPs to form H atoms (hydrogen-spillover) could reduce W^{6+}, even at mild temperatures.[40,41] In contrast, no Pt NPs were located on TiO_2; furthermore, TiO_2 requires severe reduction conditions like high pressure and high temperature.[42,43] Consequently, a high concentration of oxygen vacancies in the WO_{3-x} matrix can be achieved after H_2 treatment; these vacancies act as trapping sites for electron storage in this material (Fig. SI-4†). Moreover, the presence of oxygen vacancies is demonstrated by improved visible/NIR absorption, indicating the introduction of impurity states into the forbidden areas of the WO_3 band structure below the conduction band and a corresponding reduction in excitation energy. Solar harvesting, therefore, is significantly improved.[44,45]

The porous structures of the different samples were characterized using N_2 physical adsorption at 77 K. The specific surface area of our hollow double-shell H:Pt–WO_3/TiO_2–Au nanocomposite reaches 220 $m^2\ g^{-1}$, which is much higher than that of conventional porous TiO_2–P25 (50 $m^2\ g^{-1}$), WO_3 (8 m^2

g^{-1}), and mixed TiO_2–WO_3 (17 m^2 g^{-1}) (Table SI-1†). As far as we know, this nanocomposite has a higher surface area than any other WO_3/TiO_2 material that has been reported.[46]

The photocatalytic activity of the hollow double-shell H:Pt–WO_3/TiO_2–Au nanospheres was investigated in the photocatalytic decomposition of HCHO under visible light ($\lambda \geq 420$ nm) and in darkness, compared to those of other H_2-treated samples: hollow H:Pt–WO_3/TiO_2, hollow H:Pt–WO_3, and conventional H:Pt–WO_3, prepared from commercial WO_3 under the same catalytic conditions (see Table SI-1†). As seen in Fig. 4A, very high catalytic activity of the hollow double-shell H:Pt–WO_3/TiO_2–Au in the decomposition of HCHO was observed both under visible light and in darkness – much higher, in fact, than for other samples. More than 90% of the HCHO was converted after 6 h of reaction under visible light, and up to 80% HCHO conversion was achieved in darkness after 16 h. In addition, for hollow H:Pt–WO_3/TiO_2 and hollow H:Pt–WO_3, only 42 and 36% HCHO conversion, respectively, were obtained after 6 h under visible light, and 39 and 40% conversion, respectively, were obtained after 18 h in the dark. For the conventional H:Pt–WO_3 sample, only 10 and 5% HCHO conversion were achieved under visible light and in the dark, respectively, under the same catalytic conditions.

Fig. 4B and C show the CO_2 generation of these samples. The hollow H:Pt–WO_3/TiO_2–Au exhibits CO_2 generation of 110 and 95 μmol under 6 h of visible light illumination and 18 h in darkness, respectively, which are about 10 times higher than that of the conventional H:Pt–WO_3 (10.5 and 9 μmol, respectively) under the same catalytic conditions (Table SI-1†). The excellent catalytic activity of our hollow double-shell H:Pt–WO_3/TiO_2–Au could be attributed to its high specific surface (S_{BET} = 230 m^2 g^{-1}) compared to that of conventional H:Pt–WO_3/TiO_2 (~16 m^2 g^{-1}) and H:Pt–WO_3 (~8 m^2 g^{-1}), as well as the unique presence of Au NPs in the sample. In addition, the high surface interface between WO_3 and TiO_2 of the hollow double-shell spheres leads to an improved electron–hole charge separation, which enhances photocatalytic activity. Moreover, the H_2 treatment of the hollow double-shell spheres also has a strong impact on the catalytic performance in darkness, due to the high electron storage capacity of this sample.

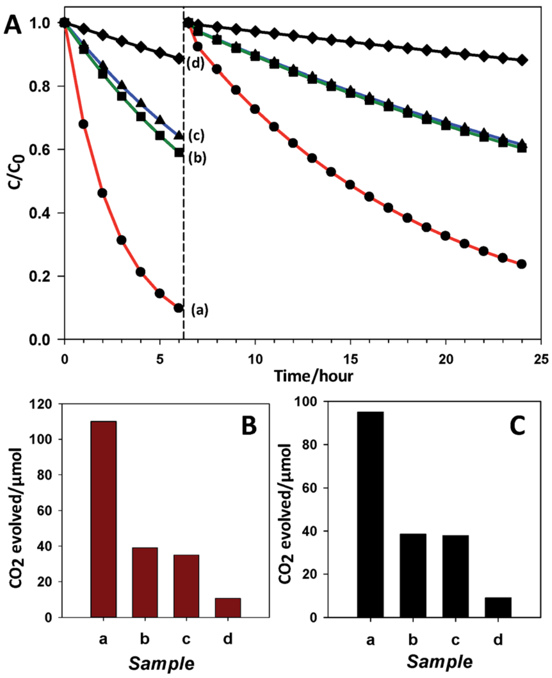

Fig. 4 (A) Degradation of HCHO as a function of reaction time under visible light illumination ($\lambda \geq 420$ nm) and in the dark; (B and C) amount of CO_2 generated over 6 h in visible light and 18 h in the dark; (a) hollow H:Pt–WO_3/TiO_2–Au; (b) hollow H:Pt–WO_3/TiO_2; (c) hollow H:Pt–WO_3; (d) conventional H:Pt–WO_3 (prepared from commercial WO_3 powders). Reaction conditions: catalysts: 50 mg; irradiated area: 4 cm^2. Light source: simulated solar light 300 W Xe lamp with 420 nm cut-off filter.

On the basis of the observed photocatalytic activities, the quantum efficiency (QE) of the prepared photocatalysts for CO_2 generation under visible light and in darkness was calculated using the following equation: QE = $N_{\text{consumed photons for }CO_2}/N_{\text{incident photons}}$; where $N_{\text{absorbed photons}}$ is the number of photons consumed for CO_2 generation and $N_{\text{incident photons}}$ is the total number of incident photons. The details of this calculation are described in the literature.[47–50] The QE for CO_2 generation by our hollow double-shell H:Pt–WO_3/TiO_2–Au is about 77.6% under visible light and in darkness. This QE is much higher than that of conventional H:Pt–WO_3 (7.7%).

As seen in Fig. 4 and Table SI-1,† in the presence of Pt, all the H_2-treated samples show high CO_2 generation, in the following order: hollow H:Pt–WO_3/TiO_2–Au > hollow H:Pt–WO_3/TiO_2 > hollow H:Pt–WO_3 > conventional H:Pt–WO_3/TiO_2 > conventional H:Pt–WO_3. It is notable that, for the samples without Pt (hollow H:WO_3/TiO_2–Au, hollow H:WO_3/TiO_2, and conventional H:WO_3), no significant CO_2 generation was observed under visible light or in darkness (Table SI-1†). Thus, the presence of Pt on WO_3 promotes the multielectron reduction of O_2 from the WO_3 conduction band despite the insufficient reduction potential of the conduction band electrons in WO_3 ($O_2 + e^- = O_2^-$ (aq), −0.284 V *vs.* NHE; $O_2 + H^+ + e^- = HO_2$ (aq), −0.046 V *vs.* NHE; +0.5 V *vs.* NHE for the WO_3 conduction band).[51] Moreover, it has been demonstrated that the $^{\bullet}OH$ radical is produced by photogenerated electrons on Pt/WO_3, rather than by photogenerated holes.[52]

It is noteworthy that this same trend is also observed in the catalytic activity of the samples without hydrogen treatment. However, their catalytic activities are much lower than those of the H_2-treated ones both under visible light and in darkness, as shown in Fig. SI-5 and Table SI-1.† It is notable that, for the hollow sample in the presence of Au, even before H_2 treatment (*e.g.*, Pt–WO_3/TiO_2–Au), the CO_2 generation rates of this sample under visible light and in darkness are much higher than those of the other samples without Au NPs. This also confirms the significant impact of Au NPs for visible light absorption on the TiO_2 surface for photocatalytic performance.

The stability of the hollow H:Pt–WO_3/TiO_2–Au nanocomposite was also studied by performing multi-recycling experiments under the same conditions. As shown in Fig. SI-6,† after five cycles (*i.e.*, 5 d of reaction), no significant change in activity was observed, indicating the high stability of our hollow

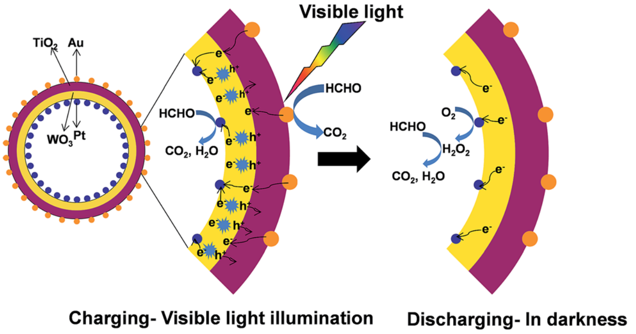

Fig. 5 Schematic illustration of the catalytic mechanism of the hollow double-shell H:Pt–WO_3/TiO_2–Au photocatalyst under visible light irradiation and in darkness.

photocatalyst in the decomposition of organic pollutants. As shown in Fig. SI-7A,† the morphology of the as-prepared sample was retained after five cycles. Also, no change in XRD patterns (Fig. SI-7B†) could be observed for the recycled samples. These results reveal that effective sunlight absorption and high charge carrier separation are required for efficient visible-light-driven photocatalysts. Also, catalytic activity in the dark depends on a number of oxygen vacancies in the WO_{3-x} matrix (Fig. SI4†), which can store electrons under light irradiation and discharge them in darkness *via* Pt NPs (as active sites) for degradation of organic pollutants.[8] Therefore, the excellent catalytic activity of our hollow double-shell H:Pt–WO_3/TiO_2–Au nanospheres under visible light and in darkness could be associated with four main factors: Pt on WO_{3-x}, high interfacial contact between WO_{3-x} and TiO_2 and specific surface area, SPR induced by Au NPs in TiO_2, and oxygen vacancies in the WO_{3-x} matrix.[43]

On the basis of these results, we propose a possible mechanism to explain the excellent photoactivity of our hollow double-shell photocomposite, as described in Fig. 5 and SI-8.† Our hollow H:Pt–WO_3/TiO_2–Au exhibits excellent performance in the degradation of HCHO. This is due to the synergetic impact of several factors. Under visible light illumination, Au NPs can harvest visible light through SPR to produce "hot" electrons at their surfaces. At the same time, electrons can be produced in the WO_{3-x} conduction band through band gap excitation. Because of suitable energy levels, the "hot" electrons are injected into the TiO_2 conduction band and then into the WO_{3-x} matrix. The photogenerated electrons can be stored in the trapping sites induced by the large amount of oxygen vacancies and simultaneously transferred to the Pt NPs for chemical reactions. In the dark, stored electrons are released and attracted by Pt NPs for the decomposition of organic compounds (Fig. 5 and SI-8†).

Conclusion

In summary, we have successfully prepared a new type of hollow double-shell H:Pt–WO_3/TiO_2–Au nanosphere using carbon colloidal spheres as the sacrificial template. The obtained photocatalyst showed excellent catalytic activity for the decomposition of HCHO under visible light and in darkness. The enhancement in catalytic activity of this new type of hollow double-shell photocatalyst can be associated with the synergic contributions of Pt NPs as a co-catalyst, the high surface area and TiO_2/WO_3 interfacial contact, plasmonic resonance effects induced by Au NPs, and a large number of oxygen vacancies in the WO_{3-x} matrix. This type of hollow material was reasonably stable under catalytic conditions, and hence, has real potential for air/water degradation both under visible-light illumination and in darkness. Work is in progress to gain further insight into the mechanistic aspects of this process. Furthermore, this strategy can be extended to other hollow double-shell nanocomposite systems for various applications.

Experimental section

Details about chemicals, synthesis of materials, characterization methods, and photocatalytic tests are available in the ESI.†

Acknowledgements

This work was supported by the Natural Science and Engineering Research Council of Canada (NSERC) through the Collaborative Research and Development with EXP Inc. (CRD) and Discovery Grants. We thank Dr Thanh-Dinh Nguyen for simulating discussion and comments.

Notes and references

1 A. Fujishima and K. Honda, *Nature*, 1972, **238**, 37–38.
2 M. Wang, J. Ioccozia, L. Sun, C. Lin and Z. Lin, *Energy Environ. Sci.*, 2014, **7**, 2182–2202.
3 F. Fresno, R. Portela, S. Suárez and J. M. Coronado, *J. Mater. Chem. A*, 2014, **2**, 2863–2884.
4 H. Wang, L. Zhang, Z. Chen, J. Hu, S. Li, Z. Wang, J. Liu and X. Wang, *Chem. Soc. Rev.*, 2014, **43**, 5234–5244.
5 M. R. Gholipour, C.-T. Dinh, F. Béland and T.-O. Do, *Nanoscale*, 2015, **7**, 8187–8208.
6 D. Su, J. Wang, Y. Tang, C. Liu, L. Liu and X. Han, *Chem. Commun.*, 2011, **47**, 4231–4233.
7 T. Tatsuma, S. Saitoh, Y. Ohko and A. Fujishima, *Chem. Mater.*, 2001, **13**, 2838–2842.
8 T. Tatsuma, S. Saitoh, P. Ngaotrakanwiwat, Y. Ohko and A. Fujishima, *Langmuir*, 2002, **18**, 7777–7779.
9 P. Ngaotrakanwiwat, T. Tatsuma, S. Saitoh, Y. Ohko and A. Fujishima, *Phys. Chem. Chem. Phys.*, 2003, **5**, 3234–3237.
10 T. Tatsuma, S. Takeda, S. Saitoh, Y. Ohko and A. Fujishima, *Electrochem. Commun.*, 2003, **5**, 793–796.
11 S. Bai, J. Jiang, Q. Zhang and Y. Xiong, *Chem. Soc. Rev.*, 2015, **44**, 2893–2939.
12 S. K. Dutta, S. K. Mehetor and N. Pradhan, *J. Phys. Chem. Lett.*, 2015, **6**, 936–944.
13 P. Christopher, H. Xin and S. Linic, *Nat. Chem.*, 2011, **3**, 467–472.
14 S. Linic, U. Aslam, C. Boerigter and M. Morabito, *Nat. Mater.*, 2015, **14**, 567–576.
15 J. Y. Park, L. R. Baker and G. A. Somorjai, *Chem. Rev.*, 2015, **115**, 2781–2817.

16 S. Sarina, E. R. Waclawik and H. Zhu, *Green Chem.*, 2013, **15**, 1814–1833.

17 X. Sun, Y. Guo, C. Wu and Y. Xie, *Adv. Mater.*, 2015, **27**, 3850–3867.

18 S. Wang, H. Qian, Y. Hu, W. Dai, Y. Zhong, J. Chen and X. Hu, *Dalton Trans.*, 2013, **42**, 1122–1128.

19 Y. Liu, L. Yu, Y. Hu, C. Guo, F. Zhang and X. Wen Lou, *Nanoscale*, 2012, **4**, 183–187.

20 C. C. Nguyen, N. N. Vu and T.-O. Do, *J. Mater. Chem. A*, 2015, **3**, 18345–18359.

21 C.-T. Dinh, M.-H. Pham, Y. Seo, F. Kleitz and T.-O. Do, *Nanoscale*, 2014, **6**, 4819–4829.

22 M.-H. Pham, C.-T. Dinh, G.-T. Vuong, N.-D. Ta and T.-O. Do, *Phys. Chem. Chem. Phys.*, 2014, **16**, 5937–5941.

23 C.-T. Dinh, Y. Seo, T.-D. Nguyen, F. Kleitz and T.-O. Do, *Angew. Chem., Int. Ed.*, 2012, **51**, 6608–6612.

24 X. Sun and Y. Li, *Angew. Chem., Int. Ed.*, 2004, **43**, 3827–3831.

25 X. Sun and Y. Li, *Angew. Chem., Int. Ed.*, 2004, **43**, 597–601.

26 J. B. Joo, Q. Zhang, I. Lee, M. Dahl, F. Zaera and Y. Yin, *Adv. Funct. Mater.*, 2012, **22**, 166–174.

27 H. Li, Z. Bian, J. Zhu, D. Zhang, G. Li, Y. Huo, H. Li and Y. Lu, *J. Am. Chem. Soc.*, 2007, **129**, 8406–8407.

28 C.-T. Dinh, H. Yen, F. Kleitz and T.-O. Do, *Angew. Chem., Int. Ed.*, 2014, **53**, 6618–6623.

29 D. Ding, K. Liu, S. He, C. Gao and Y. Yin, *Nano Lett.*, 2014, **14**, 6731–6736.

30 S. J. Moniz, S. A. Shevlin, D. J. Martin, Z.-X. Guo and J. Tang, *Energy Environ. Sci.*, 2015, **8**, 731–759.

31 M. P. Casaletto, A. Longo, A. Martorana, A. Prestianni and A. M. Venezia, *Surf. Interface Anal.*, 2006, **38**, 215–218.

32 H. G. Yang, C. H. Sun, S. Z. Qiao, J. Zou, G. Liu, S. C. Smith, H. M. Cheng and G. Q. Lu, *Nature*, 2008, **453**, 638–641.

33 K. B. Narayanan and N. Sakthivel, *Mater. Lett.*, 2008, **62**, 4588–4590.

34 X.-L. Li, T.-J. Lou, X.-M. Sun and Y.-D. Li, *Inorg. Chem.*, 2004, **43**, 5442–5449.

35 N. Serpone, D. Lawless and R. Khairutdinov, *J. Phys. Chem.*, 1995, **99**, 16646–16654.

36 L. Cheng, X. Zhang, B. Liu, H. Wang, Y. Li, Y. Huang and Z. Du, *Nanotechnology*, 2005, **16**, 1341.

37 W. C. Conner and J. L. Falconer, *Chem. Rev.*, 1995, **95**, 759–788.

38 J.-Y. Eom, S.-J. Lim, S.-M. Lee, W.-H. Ryu and H.-S. Kwon, *J. Mater. Chem. A*, 2015, **3**, 11183–11188.

39 T.-D. Nguyen-Phan, S. Luo, Z. Liu, A. D. Gamalski, J. Tao, W. Xu, E. A. Stach, D. E. Polyansky, S. D. Senanayake and E. Fujita, *Chem. Mater.*, 2015, **27**, 6282–6296.

40 S. Khoobiar, *J. Phys. Chem.*, 1964, **68**, 411–412.

41 R. Prins, *Chem. Rev.*, 2012, **112**, 2714–2738.

42 X. Yu, B. Kim and Y. K. Kim, *ACS Catal.*, 2013, **3**, 2479–2486.

43 X. Chen, L. Liu, P. Y. Yu and S. S. Mao, *Science*, 2011, **331**, 746–750.

44 R. Wu, J. Zhang, Y. Shi, D. Liu and B. Zhang, *J. Am. Chem. Soc.*, 2015, **137**, 6983–6986.

45 J. Yan, T. Wang, G. Wu, W. Dai, N. Guan, L. Li and J. Gong, *Adv. Mater.*, 2015, **27**, 1580–1586.

46 G. Puma, *Chem. Commun.*, 2007, 4749–4751.

47 M. Liu, X. Qiu, M. Miyauchi and K. Hashimoto, *J. Am. Chem. Soc.*, 2013, **135**, 10064–10072.

48 M. Liu, R. Inde, M. Nishikawa, X. Qiu, D. Atarashi, E. Sakai, Y. Nosaka, K. Hashimoto and M. Miyauchi, *ACS Nano*, 2014, **8**, 7229–7238.

49 J. M. Buriak, P. V. Kamat and K. S. Schanze, *ACS Appl. Mater. Interfaces*, 2014, **6**, 11815–11816.

50 H. Kisch and D. Bahnemann, *J. Phys. Chem. Lett.*, 2015, **6**, 1907–1910.

51 R. Abe, H. Takami, N. Murakami and B. Ohtani, *J. Am. Chem. Soc.*, 2008, **130**, 7780–7781.

52 J. Kim, C. W. Lee and W. Choi, *Energy Environ. Sci.*, 2010, **44**, 6849–6854.

Supporting Information

Efficient hollow double-shell photocatalysts for the degradation of organic pollutants under visible light and in darkness

*Chinh- Chien Nguyen, Nhu- Nang Vu, and Trong- On Do**

Experimental Section

Chemicals

Sucrose, sodium tungstate, hexachloroplatinic acid hexahydrate, titanium butoxide (TB), benzyl alcohol (BA), oleylamine (OM), benzyl ether, tetraethylammonium hydroxide (TEAOH), polyethyleneimine (PEI), ammonium hydroxide, and tetrachloroauric(III) acid were purchased from Aldrich. All of the reagents were used without further purification.

Synthesis of carbon colloidal spheres@Pt-WO_3:

Typically, 32 g sucrose was dissolved in 160 mL deionized water. Then, 0.5 g Na_2WO_4 and 2 g of a 1 mg mL^{-1} H_2PtCl_6 aqueous solution was added to the above solution, which was then heated in a Teflon-lined autoclave at 160 °C for 6 h. Afterwards, the solid product was collected by centrifugation at 6000 ppm for 10 min, washed several times with water and ethanol, and dried overnight at 80 °C.

Synthesis of titanate nanodisks (TNDs):

The synthesis of water-soluble TNDs was based on our previous studies. Briefly, 2g of TB, 12 g of OM, 12g of BA, and 30g of benzyl ether were added to a 100-mL round-bottom flask. The reaction mixture was heated to 190 °C at the heating rate 5 °C/min under nitrogen flow. After 20 h, the reaction was cooled to room temperature. After addition of excess absolute ethanol, the TNDs were recovered and were subjected to three cycles of dispersion in toluene and re-precipitation with ethanol. Then, the as-synthesised TNDs were treated with a mixture of TEAOH (15 mmol), ethanol (15 ml), and water (15 ml). The mixture was stirred overnight at room temperature followed by adding of acetone to obtain precipitate TNDs. Afterwards, the precipitate was washed several times with acetone and finally dispersed in 100 mL of water.

Synthesis of Carbon colloidal spheres@Pt-WO_3/TNDs-$AuCl_4^-$

As-prepared carbon colloidal spheres@Pt-WO_3 were coated with TNDs using a layer-by-layer deposition technique (see Scheme SI 2). The carbon colloidal spheres@Pt-WO_3 (2 g) was dispersed in 50 mL of deionized water containing 0.3 g PEI and stirred for 1 h to ensure the saturated adsorption of PEI on the surface of the carbon spheres. Excess PEI was removed by centrifugation before being subjected to 50 mL of H_2O containing 50 mg TNDs under stirring. The electrostatic force between the negatively charged TNDs and positively charged PEI on the surface of carbon spheres obtains a layer of TNDs on the surface of carbon spheres. The resulting material was then recovered by centrifugation and washing. The above procedure was repeated for seven cycles to obtain the carbon colloidal spheres@Pt-WO_3/TNDs. Then, as-prepared carbon colloidal spheres@Pt-WO_3/TNDs was re-dispersed in 50 mL of $HAuCl_4$ solution (15 mM). The resulting mixture was stirred for 1 h to ensure the adsorption of $AuCl_4^-$ on the carbon colloidal spheres@Pt-WO_3/TNDs. After that the precipitate was collected by centrifugation, dried at 70 °C overnight and calcined at 550 °C for 3 h to obtain hollow double-shell Pt-WO_3/TiO_2-Au.

Hydrogen treatment

The calcined hollow double-shell Pt-WO_3/TiO_2-Au spheres (100 mg) were put into a ceramic boat and treated in a hydrogen atmosphere (95% in Argon) in a tube furnace at 350 °C at a flow rate 200 mL min^{-1} for 1 h to obtain hollow double-shell H_2-treated Pt-WO_3/TiO_2-Au spheres (denoted as H: Pt-WO_3/TiO_2-Au).

Characterisation

TEM images of the samples were obtained on a JOEL JEM 1230 operated at 120 kV. High-resolution TEM (HRTEM) images were obtained on Philips G2 F30 Tecnai instrument operated at 300 kV. SEM images were obtained on a JEOL 6360 instrument operated at 15 kV. Powder XRD patterns of the samples were obtained on a Bruker SMART APEXII X-ray diffractometer equipped with a Cu Kα radiation source (λ = 1.5418 Å). XPS measurements were carried out in an ion-pumped chamber (evacuated to 10^{-9}Torr) of a photoelectron spectrometer (Kratos Axis-Ultra) equipped with a focused X-ray source (Al Kα, hν = 1486.6 eV). The UV-vis spectra were recorded on a Cary 300 Bio UV-visible spectrophotometer. N_2 adsorption–desorption isotherms of the samples were obtained at −196 °C using Quantachrome Autosorb-1 MP analyser. Before the measurements, the samples were outgassed under vacuum for 6 h at 120 °C.

Catalytic test

Photocatalytic decomposition of formaldehyde: The photocatalytic reactions were conducted in a home-built top-irradiated reactor (~250 cm^3) at ambient temperature and atmospheric pressure. For this photocatalytic reactor system, the optimum amount of photocatalysts according to our hollow type of nanocomposites was done to be ∼50 mg.[1] In a typical photocatalytic experiment, an optimized amount of photocatalyst (50 mg) was spread uniformly in a Petri dish with an inner diameter of 2.2 cm and placed at the bottom of the reactor. The reaction cell was then evacuated, and filled with fresh synthetic air. Then, a certain amount of condensed formaldehyde solution (37%) was injected into the reactor. Prior to light irradiation, the reaction cell was kept in the dark for four hours to ensure that an adsorption–desorption equilibrium of the reactant was established on the surface of the photocatalysts. Then, the reactor was illuminated with visible light ($\lambda \geq 420$ nm) through a cut-off filter from a solar simulator 300-W Xe lamp, for six hours. Light intensity was measured by a light radiometer (Newport). Afterwards, the reaction cell was evacuated, filled with fresh synthetic air before injecting a certain amount of condensed formaldehyde solution, and was kept in the dark for 18 h. The initial concentration of HCHO vapour after adsorption/desorption equilibrium was controlled at about 130±5 µmol. Formaldehyde concentration in the reactor was conducted on-line with a HCHO monitor (Photoacoustic Gas Monitor INNOVA 1412i). Amounts of CO_2 gas generated under visible illumination and in darkness were analysed by a gas chromatograph (Agilent 7820A) equipped with a thermal conductivity detector (TCD) with carboxen-1010 capillary column and He as the gas carrier.

Quantum efficiency (QE) calculation

The calculation of quantum efficiency (QE) was conducted using the same procedure reported in the literature.[1, 2] Under the visible light irradiation, the wavelength of visible light is from 420 to 700 nm, and the number of incident photons by integration of intensity at each wavelength is $7.4\text{x}10^{15}$ photon.$s^{-1}cm^{-2}$. The irradiating area is 4 cm^2. The optimized irradiation time is 6 hours. Therefore, the number of incident photons for 6h was calculated by using the following equations:

$N_{\text{incident photons}} = 7.4\text{x}10^{15}\text{x}4\text{x}6\text{x}3600=6.393\text{x}10^{20}$ photons.

For CO_2 generation, assuming that the reactions from HCHO to CO_2 are proceeded on hollow double shell H:Pt-WO_3/TiO_2-Au as: $HCHO+O_2+4H^++4e- \rightarrow CO_2 + 3H_2O$ ($2e^-_{CB} + O_2 + 2H^+ \rightarrow H_2O_2$; $HCHO + 2H_2O_2 \rightarrow CO_2 + 3H_2O$); $2H_2O + 4h^+ \rightarrow O_2 + 4H^+$.[3-6] Thus, four photons are required to produce one CO_2 molecule. n_{CO2} was determined to be 110 µmol and 96 µmol under visible irradiation and darkness, respectively. Therefore, the number of photons consumed to produce CO_2 molecules both under 6 hours of light illumination and 18 hours in darkness:

$N_{\text{consumed photons for CO2}} = 4 \text{ x } (110 + 96) \text{ x } 10^{-6} \text{ x } 6.023\text{x}10^{23} = 49.62 \text{ x } 10^{19}$

$QE = N_{\text{consumed photons for CO2}}/N_{\text{incident photons}} = (49.62\text{x}10^{19}/6.393\text{x}10^{20}) \text{ x } 100 = 77.6\%$

References

1. M. Liu, X. Qiu, M. Miyauchi and K. Hashimoto, *Journal of the American Chemical Society*, 2013, **135**, 10064-10072.
2. M. Liu, R. Inde, M. Nishikawa, X. Qiu, D. Atarashi, E. Sakai, Y. Nosaka, K. Hashimoto and M. Miyauchi, *ACS nano*, 2014, **8**, 7229-7238.
3. J. Kim, C. W. Lee and W. Choi, *Environmental science & technology*, 2010, **44**, 6849-6854.
4. M. Pelaez, N. T. Nolan, S. C. Pillai, M. K. Seery, P. Falaras, A. G. Kontos, P. S. Dunlop, J. W. Hamilton, J. A. Byrne and K. O'Shea, *Applied Catalysis B: Environmental*, 2012, **125**, 331-349.
5. L. G. Devi and R. Kavitha, *Applied Catalysis B: Environmental*, 2013, **140–141**, 559-587.
6. P. Ngaotrakanwiwat, T. Tatsuma, S. Saitoh, Y. Ohko and A. Fujishima, *Physical Chemistry Chemical Physics*, 2003, **5**, 3234-3237.

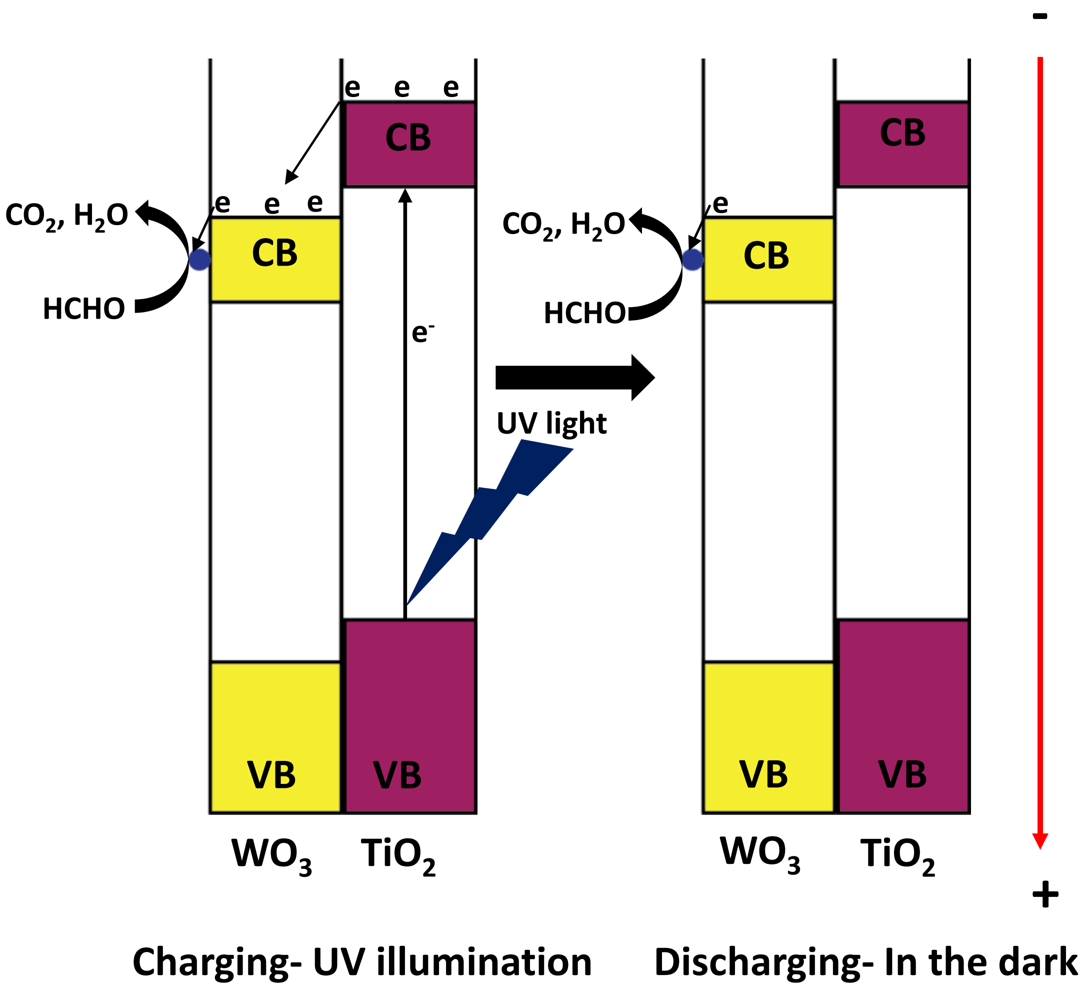

Scheme SI-1. Illustration of conventional WO_3/TiO_2 nanocomposite under UV illumination and in darkness; the catalytic activity depends on UV irradiation and interfacial contact between WO_3 and TiO_2, whereas the activity in darkness is effected by electron transfer from TiO_2 and oxygen vacancies in the WO_3 structure. For these reasons, this conventional nanocomposite shows low activity under visible irradiation and in the dark.

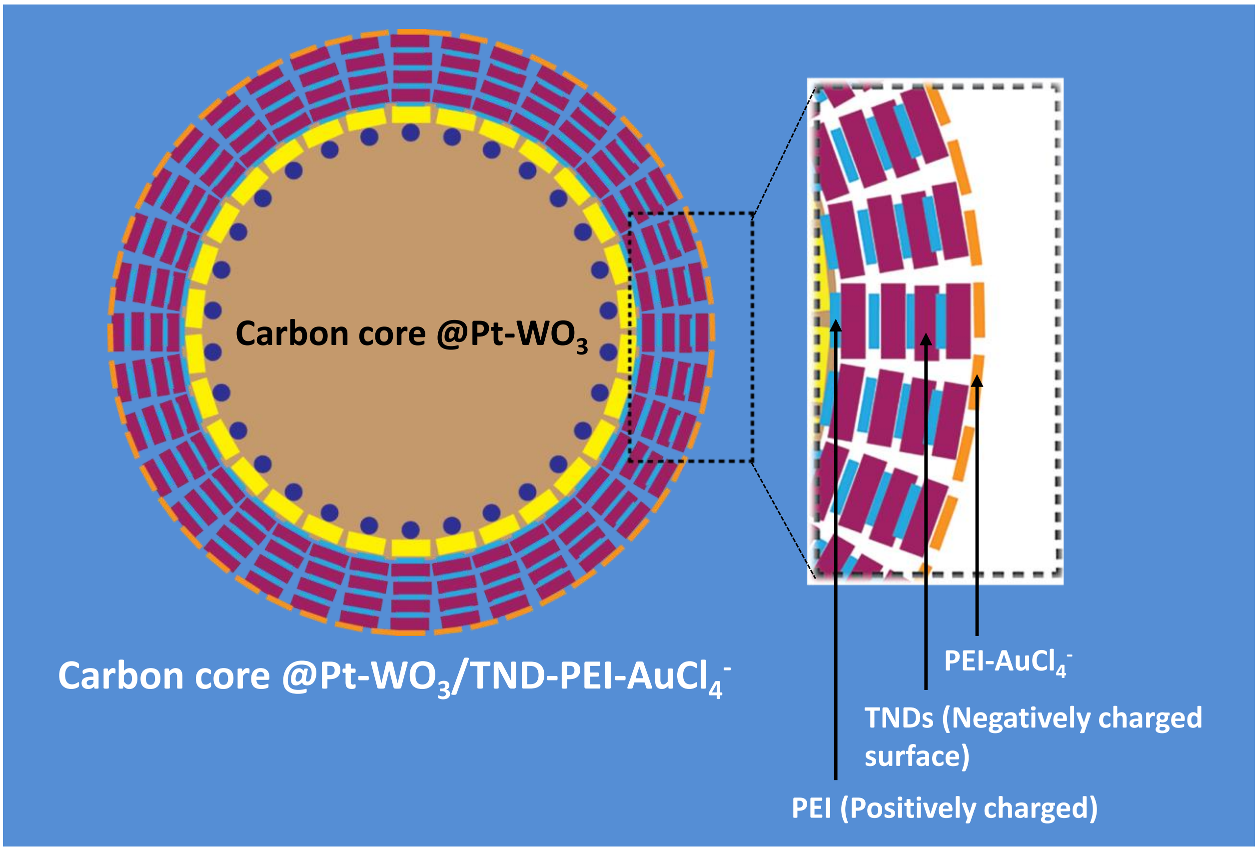

Scheme SI 2. Illustration of TNDs coated on carbon spheres@ Pt-WO_3 using layer-by-layer technique

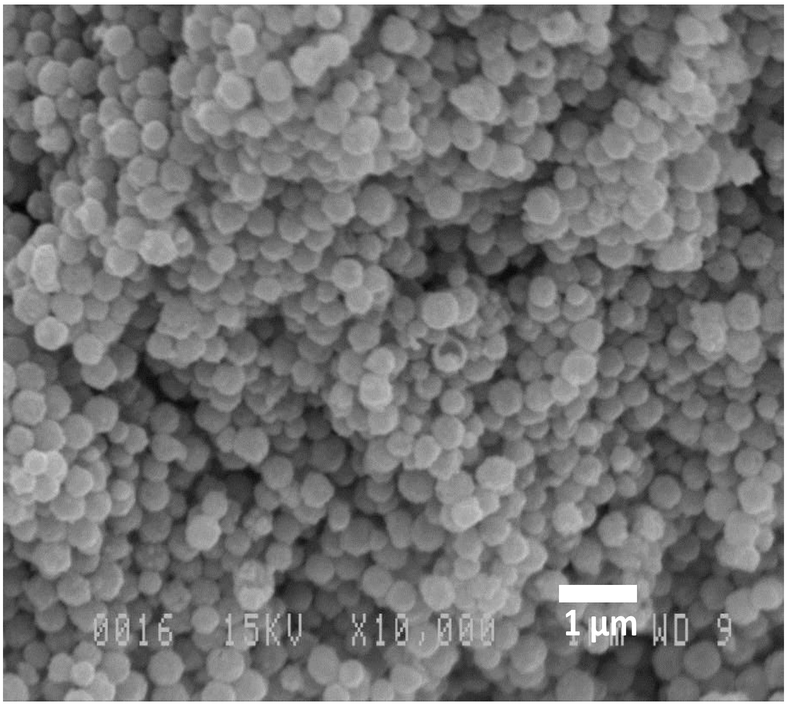

Figure SI 1. SEM of the hollow H:Pt-WO_3 nanospheres

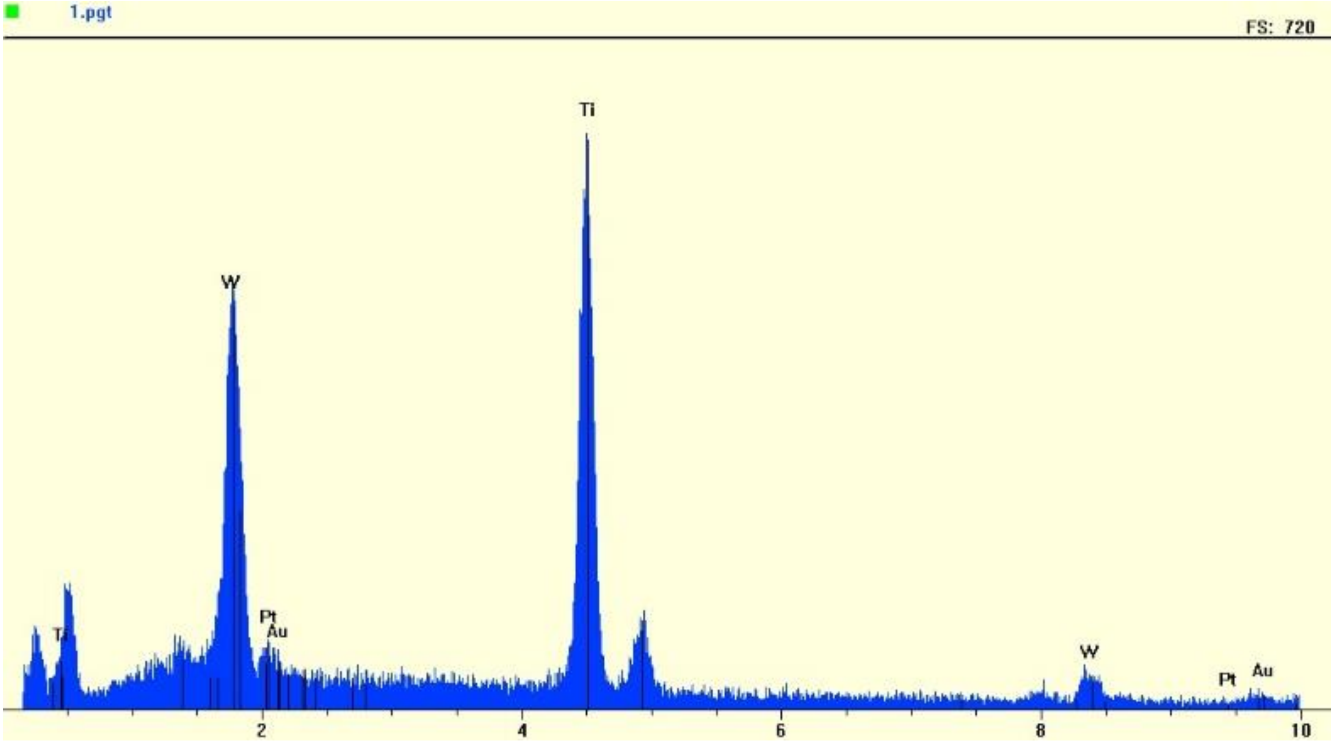

Figure SI 2. EDS of hollow H:Pt-WO_3/TiO_2-Au spheres confirms the presence of Pt, W, Ti, and Au in the sample.

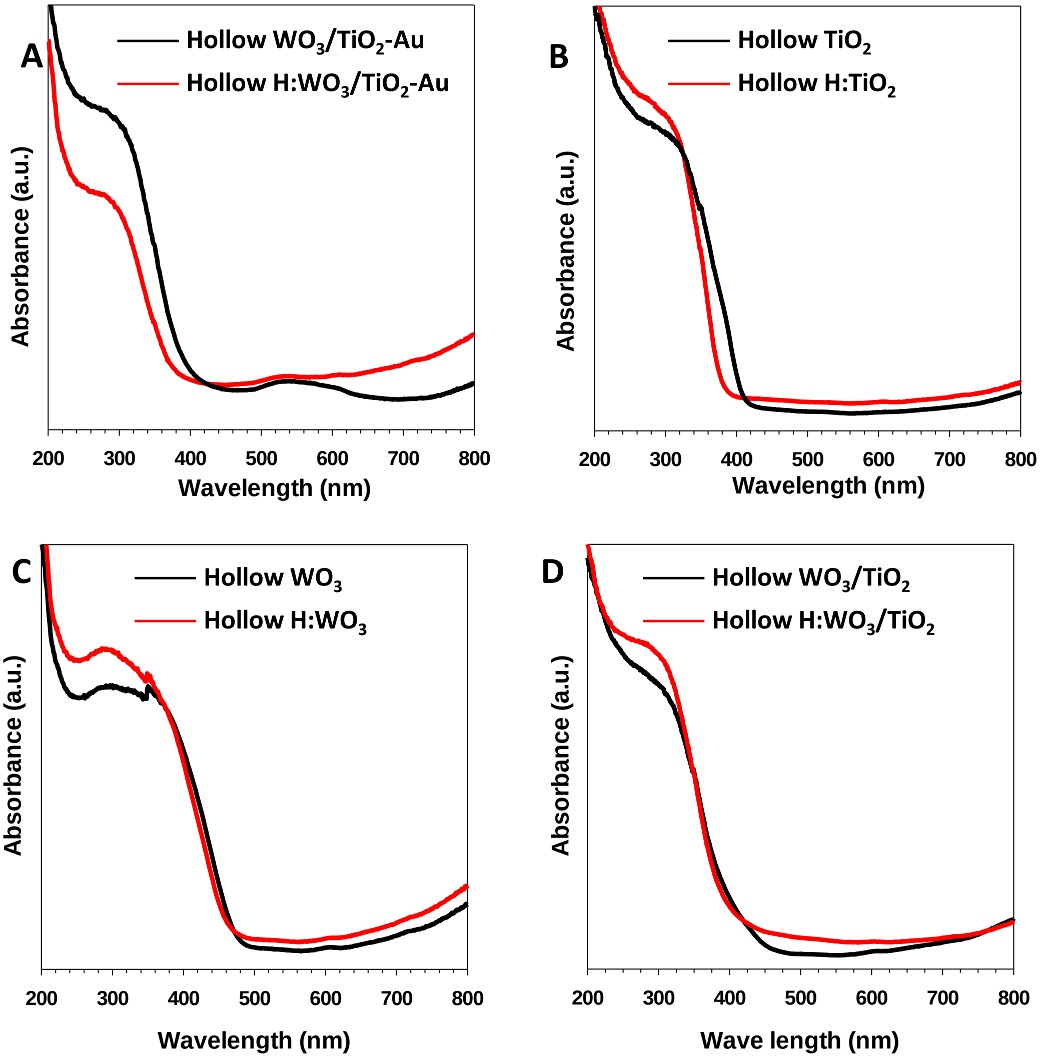

Figure SI 3. UV-Visible spectra of different samples in the absence of Pt before and after H_2 treatment; It should be noted that no significant improvement in light absorption occurs before and after H_2 treatment.

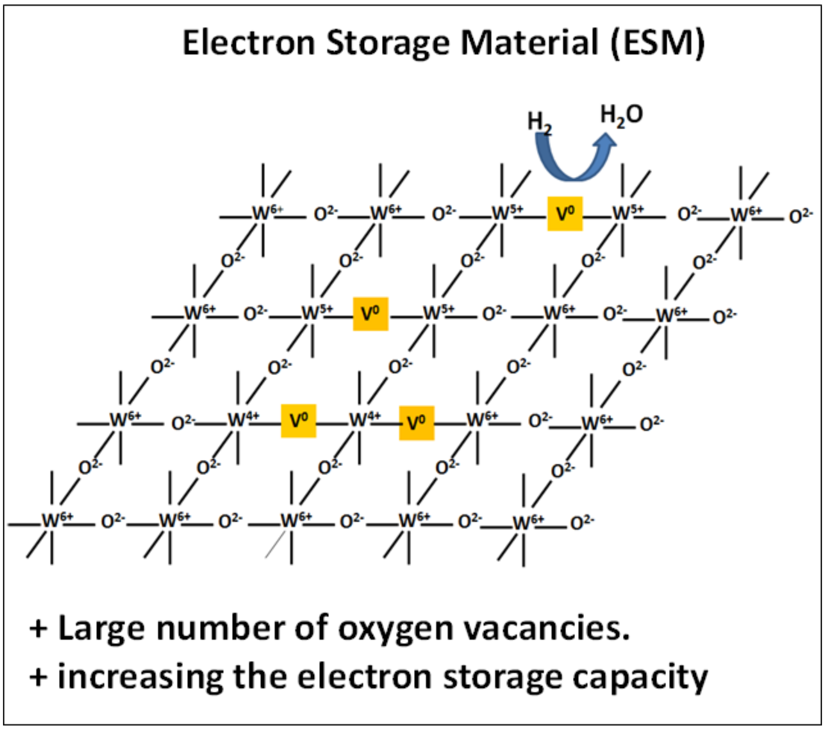

Figure SI 4. Illustration of oxygen vacancies in the WO_3 structure after H_2 treatment enhancing light absorption and electron storage capacity.

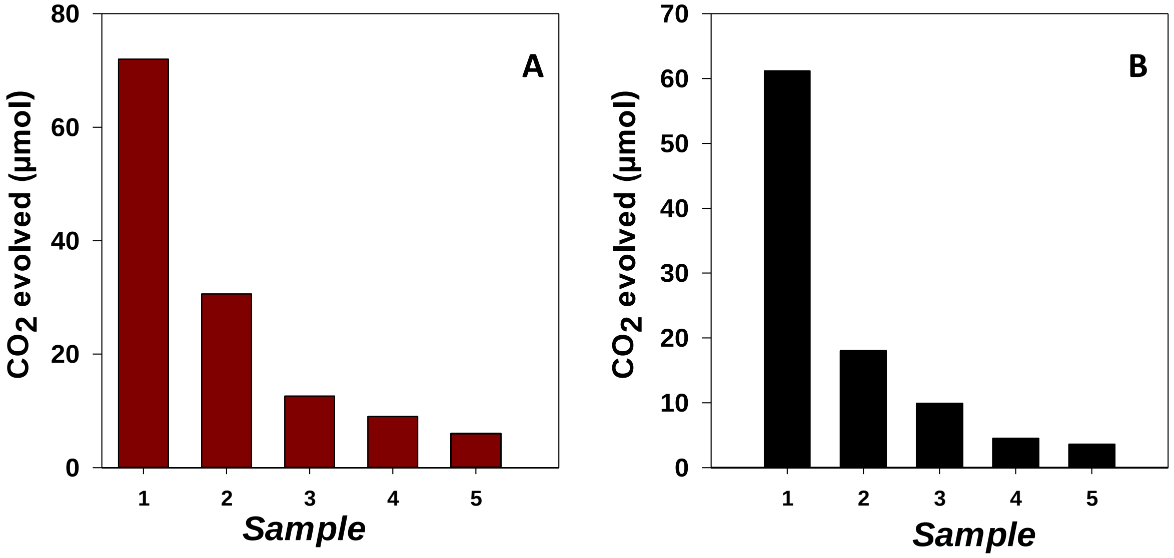

Figure SI 5. CO_2 generation rates of the samples under visible illumination (red colour) and in darkness (black colour) before hydrogen treatment (A and B) (1) hollow Pt-WO3/TiO_2-Au spheres; (2) hollow Pt-WO_3/TiO_2; (3) hollow Pt-WO_3; (4) conventional Pt-WO_3/TiO_2, prepared from commercial WO_3 and TiO2-P25, (5) conventional Pt-WO_3 prepared from commercial WO_3.

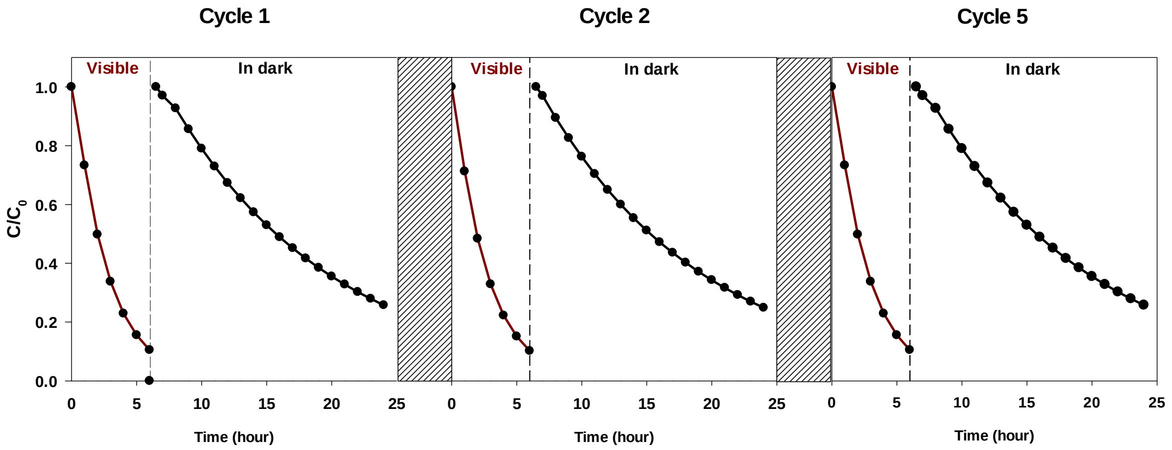

Figure SI 6. Catalytic stability of hollow H_2-treated Pt-WO_3/TiO_2-Au nanospheres for degradation of formaldehyde over five cycles under visible light and in darkness.

Table SI 1. Summaries of specific surface area and CO_2 generation rate of different samples before and after hydrogen treatment for formaldehyde (HCHO) decomposition under visible-light and in darkness.

Sample	Surface area ($m^2.g^{-1}$)	Rate of CO_2 generation under 6h visible light (μmol)	Rate of CO_2 generation 18h in the dark (μmol)
Hollow H:Pt-WO_3/TiO_2-Au	220	**110**	**96**
Hollow Pt-WO_3/TiO_2-Au	230	72	61
Hollow H:Pt-WO_3/TiO_2	230	39	38.7
Hollow Pt-WO_3/TiO_2	240	30.6	18
Hollow H:Pt-WO_3	25	35.1	37.8
Hollow Pt-WO_3	26	12.6	9.9
Hollow H:WO_3/TiO_2-Au	235	ND	ND
Hollow H:WO_3/TiO_2	240	ND	ND
Hollow H:WO_3	24	ND	ND
Conventional H:Pt-WO_3/TiO_2-Au	13	25.7	12.4
Conventional Pt-WO_3/TiO_2-Au	13	18.6	9.3
Conventional H:Pt-WO_3/TiO_2	16	13.5	8.1
Conventional Pt-WO_3/TiO_2	17	9	4.5
Conventional H:Pt-WO_3	08	**10.5**	**9**
Conventional Pt-WO_3	08	6	3.6
Commercial TiO_2 -P25	50	ND	ND

″ND”: not detected

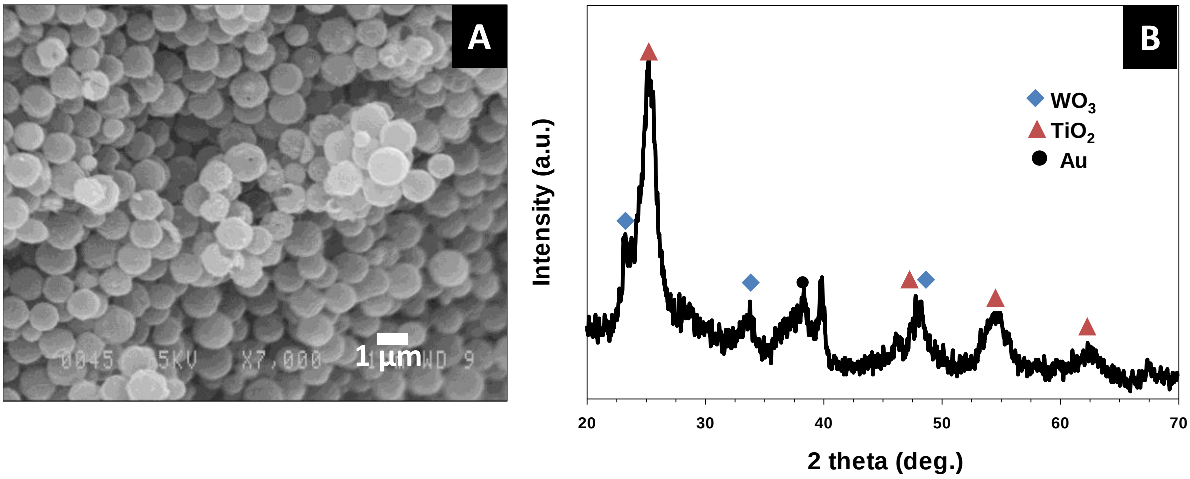

Figure SI 7. A) SEM images and XRD pattern (B) of the hollow H: Pt-WO_3/TiO_2-Au after the fifth cycle.

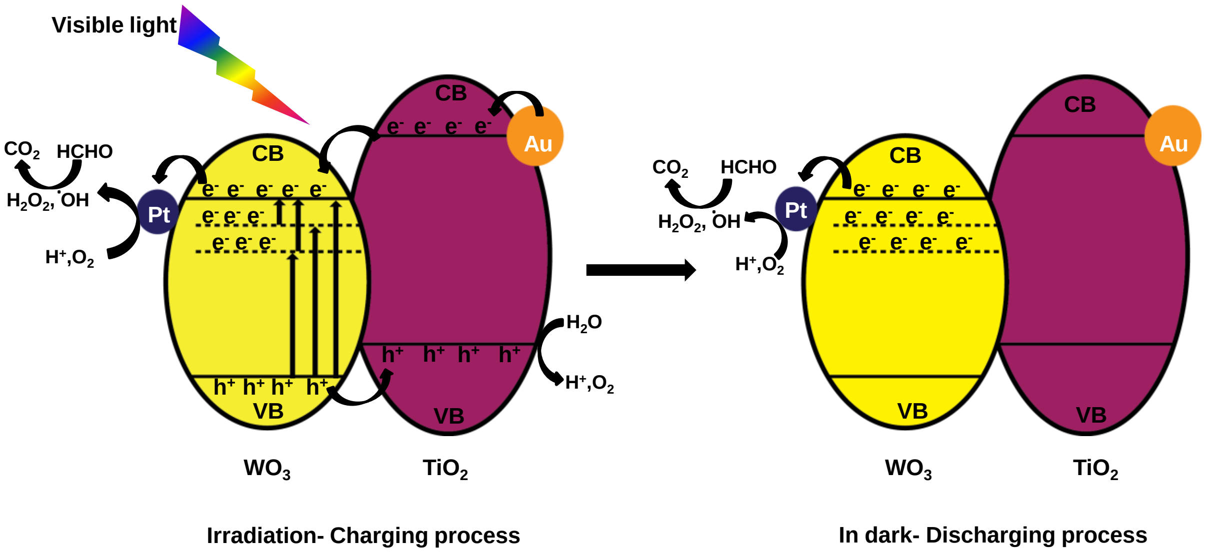

Figure SI 8. Schematic of hollow H:Pt-WO_3/TiO_2-Au with strong sunlight absorption, high surface area, and high concentration of oxygen vacancies.